Molecular Based Mathematical Biology
Research Article

Open Access

Shixin Xu, Minxin Chen*, Sheereen Majd, Xingye Yue, and Chun Liu

Modeling and Simulating Asymmetrical Conductance Changes in Gramicidin Pores

Abstract: Gramicidin A is a small and well characterized peptide that forms an ion channel in lipid membranes. An important feature of gramicidin A (gA) pore is that its conductance is affected by the electric charges near the its entrance. This property has led to the application of gramicidin A as a biochemical sensor for monitoring and quantifying a number of chemical and enzymatic reactions. Here, a mathematical model of conductance changes of gramicidin A pores in response to the presence of electrical charges near its entrance, either on membrane surface or attached to gramicidin A itself, is presented. In this numerical simulation, a two dimensional computational domain is set to mimic the structure of a gramicidin A channel in the bilayer surrounded by electrolyte. The transport of ions through the channel is modeled by the Poisson-Nernst-Planck (PNP) equations that are solved by Finite Element Method (FEM). Preliminary numerical simulations of this mathematical model are in qualitative agreement with the experimental results in the literature. In addition to the model and simulations, we also present the analysis of the stability of the solution to the boundary conditions and the convergence of FEM method for the two dimensional PNP equations in our model.

Keywords: Gramicidin; conductance change; finite element method; Poisson-Nernst-Planck (PNP) equation; ion channels

DOI 10.2478/mlbmb-2014-0003
Received December 20, 2013; accepted March 21, 2014.

1 Introduction and background

Gramicidin A (gA) is a well characterized short polypeptide of about hundreds of atoms with a helix structure. This peptide is relatively easy to be synthesized and manipulated, compared with a typical sodium channel which has thousands of atoms. GA is also relatively stable, and, therefore, have been widely applied in biochemical and biophysical studies. Upon head to head dimerization, gramicidin A forms an elongated channel in lipid bilayers that is permeable to small monovalent cations [47](see (a) in Fig. 1). In experiments, with the application of a voltage difference across the lipid bilayer, ions pass through the gramicidin A channel, and amplitudes of current and conductance of the channel can be measured electrically [2]. One of the most important features of gramicidin A channel is that the current and the conductance of the channel are greatly affected by the environment near the entrance of the gramicidin A pores [3], such as the charge densities of

Shixin Xu: Center for System Biology, Department of Mathematics, Soochow University, Suzhou 215006, China, E-mail: xsxztr@hotmail.com
***Corresponding Author: Minxin Chen:** Center for System Biology, Department of Mathematics, Soochow University, Suzhou 215006, China, E-mail: chenmx@gmail.com
Sheereen Majd: Department of Bioengineering, Department of Engineering Science and Mechanics Pennsylvania State University, University Park, PA 16802, US
Xingye Yue: Center for System Biology, Department of Mathematics, Soochow University, Suzhou 215006, China, E-mail: xyyue@suda.edu.cn
Chun Liu: Department of Mathematics, Pennsylvania State University, University Park, PA 16802, US, E-mail: liu@math.psu.edu

the solvent, the surface charge of membrane surrounding the channel, and charged functional groups attached to gramicidin A. This unique feature has led to the application of gramicidin A pores as biosensors for changes of local environments. For instance, in a recent study, gramicidin A pores were applied to detect and quantify the activities of membrane active enzymes phospholipase D (PLD) and phospholipase C (PLC) on planar lipid bilayers rapidly by measuring the conductance changes of gramicidin A pores [28]. These enzymes catalyze the hydrolysis of certain ester bonds in phospholipids and, in many lipid substrates, lead to a change in the net electrical charge of the lipid. In the case of PLD, which hydrolyzes electrically neutral phosphatidylcholine (PC) and produces negatively charged phosphatidic acid (PA), the change in membrane surface charge leads to an accumulation of cations close to the membrane surface and hence, a significant increase in magnitude of current and conductance of the channel. Given the fact that the gramicidin A conductance is affected by the electric charges present near its entrance and not by those charges near its exit, these authors were able to show that if PLD is exposed only to one side of bilayer, gramicidin A conductance will change **asymmetrically** [28]. More specifically, when the polarity of the applied voltage was such that the entrance of pore was placed with the negatively charged leaflet, due to the activity of PLD, the conductance of gramicidin A increased over time dramatically, while the conductance almost stayed unchanged when the polarity was such that the entrance of the pore was placed with the leaflet that carried no charge, since it was not in contact with PLD. Others have explored application of chemically-modified gramicidin As, by attachment of different functional charged groups such as sulfonate, amine, and phosphate, for sensing chemical and enzymatic reactions around gramicidin A channels [6, 25]. In another intriguing study, engineered gramicidin As that carried charged groups was used to control the conductance of pore [25, 27] and create an ionic diode [26]. The authors showed that dimerization of two different charged trimethylgramicidine monomers (positively charged gA-NMe_3^+ and negative charged gA-T^-) results in the formation of channels with asymmetric conductance. In this paper, we will model the asymmetrical changes in gramicidin A conductance that have been reported in these studies.

The transport of ionic particles through ion channels is by nature a multiscale-multiphysics system. It couples the structure of the protein channels with the electrostatics, as well as diffusion and convection. Over the past decades, in addition to the enormous experimental efforts, many theoretical models and computational methods at different scales have been developed to understand the transport of ionic fluids and the mechanism of ion channels. At atomic scales, molecular dynamics (MD) and stochastic models are the most widely used tools to simulate the channel systems. Molecular dynamics simulations treat the interactions between all atoms explicitly by using atomistic interaction potential, and evolve the configurations of whole system under the Newton's second law. Due to the computational complexity and cost, it is difficult to reach the time scale of determining the ion fluxes through the channel using molecular dynamics simulation. Among the stochastic models, Brownian dynamics (BD) is a common way that extends the simulation scale by incorporating the solvent implicitly through inducing the friction tensor and stochastic forces. The Brownian dynamics simulations have been successfully used to simulate a number of biological and physiological systems [40], such as the ion permeation in biological pores such as porin channels [41], potassium channel [1] and channel VDAC [21].

At continuum scale, the coupled Poisson-Nernst-Planck (PNP) system theory is a well-established model for studying the ion distribution and transport under the gradients of concentration and the electrical field [13]. Many computational methods have been employed for solving the Poisson-Nernst-Planck equations of ion channel systems, such as finite differences method [20, 51, 53, 54], finite element method [23, 45], spectral element method [16], and finite volume method [30]. It has been demonstrated that the PNP simulations and BD simulations produce comparable results for OmpF and α-Hemolysin channel [19, 32]. While the size of gramicidin A pore is on the scale of Å, the continuous description of PNP and PNP like theory can still capture many realistic physical and biological properties. One justification of this may lie in the fact that while the size of pore is comparable to the ion size, the time scale of an ion particle moving through the channel is far shorter than the usual time scale of relevant biological time scale of 10^{-3} seconds. In fact, it can be shown that the PNP system can be rigorous derived as long time limit of kinetic descriptions or particle descriptions [48].

The objective of this paper is to qualitatively model and simulate the conductance of gramicidin A pores in the presence of electrical charges near the channel. With a two-dimensional computational domain set for a single gramicidin A channel in a bilayer lipid membrane, Poisson-Nernst-Planck equations are used to model the ion-transport in the gramicidin A channel. This work considers the effects of electronic charges present on the membrane surface (eg. charged lipids) as well as those charges attached to the gramicidin A (e.g. chemically modified gramicidin As with charged group attachments). The experimental results from the literatures are reproduced by solving Poisson-Nernst-Planck equations numerically using Finite Element Methods (FEM).

This paper is organized as follows. In the second section, we present the mathematical model of ion-transport in gramicidin A pore, including the Poisson-Nernst-Planck equations, parameters and geometry setting. The analysis of the stability of the solutions to the jump conditions is also presented in this section. In the third section, Finite element method for solving Poisson-Nernst-Planck equations and corresponding analysis of convergence are discussed. The computational results and comparisons with experimental results are shown in the Results section. The final section gives some concluding remarks.

2 Modeling and theoretical settings

2.1 The computational domain

In our mathematical model, a two dimensional 120 Å × 40 Å simulation box Ω is set as the computational domain (see Fig. 1). Here, the origin of coordinates is placed at the center of box. The box has a macromolecule part Ω_m and a solvent region Ω_s. The macromolecule part Ω_m consists of the membrane represented by two slabs and the gramicidin A that is represented by two ellipses:

$$\frac{(y-y_i)^2}{b^2}+\frac{(x-x_i)^2}{a^2}=1, i=1,2, \tag{1}$$

where $(x_1, y_1) = (0, 2\ \text{Å})$ and $(x_2, y_2) = (0, -2\ \text{Å})$ are the centers of the ellipses, $a = 20$ Å and $b = 1/2$ Å are the major and minor radiuses, respectively. are used to simulate the geometry property of real protein in the channel which is wider at the entrance and exit of the channel, and thinner in the middle part. Ω_I is the channel region in the solvent region Ω_s. The geometries of the computational domain, especially the thickness of the membrane, the width and length of the channel are critical for reproducing the conductance changes of channel measured experimentally. It should be noted that due to our 2-D setting in this paper, the geometry of gramicidin A is only through the width and length. In our simulations, the sizes of the channel and membrane are set to be comparable with the real sizes of gramicidin A and lipid layer. The thickness of the bilayer is 40 Å [52]. In solvent region Ω_s, the channel region Ω_I is from $x = -40/3$ Å to $x = 40/3$ Å along the x direction, corresponding to a length of 2.6 nm, and the width of the pore at $x = 0$ is 3 Å [47]. As shown in Fig. 2, the boundary of simulation box is denoted by $\partial\Omega$ and the interface between the solvent and macromolecule is Γ=$\Gamma_1 \bigcup \Gamma_2$, where Γ_1 is the boundary of membrane and Γ_2 is the boundary of gramicidin A exposed to the solvent.

2.2 Continuum descriptions of ion transport

We use the Poisson-Nernst-Planck equations to model the ion transport in the ion channel. The Poisson-Nernst-Planck equations can be derived using the Energetic Variational Approach [12, 14, 38]. This approach is based on the concepts: Newton's force balance law, Least Action Principle [43], Maximum Dissipation Principle [33, 34], and energy dissipation law $\frac{dE^{total}}{dt} = -\Delta$. Here $E^{total} = \mathcal{K} + \mathcal{F}$, $\mathcal{K}$ is kinetic energy, $\mathcal{F} := \mathcal{U} - \mathcal{TS}$ is the Helmholtz free energy with internal energy $\mathcal{U}$, temperature $\mathcal{T}$ and entropy $\mathcal{S}$. As in the standard statistical physics, the particles interactions contribute to the internal energy $\mathcal{U}$. These interactions can be local, such as hard core interactions or nonlocal, such as Coulomb electro static interactions. Δ is the dissipation

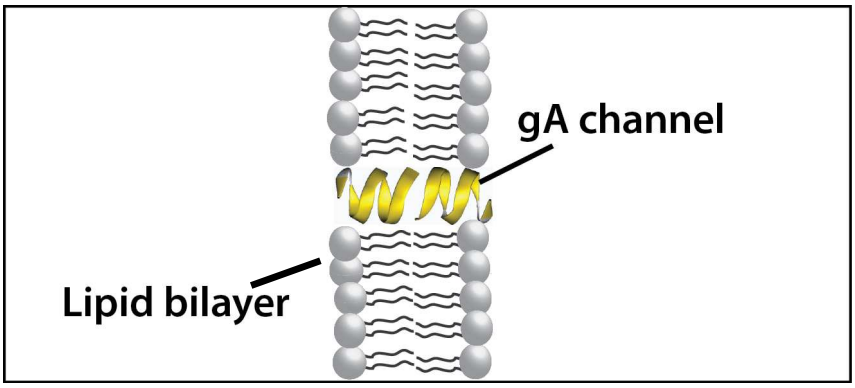

(a)

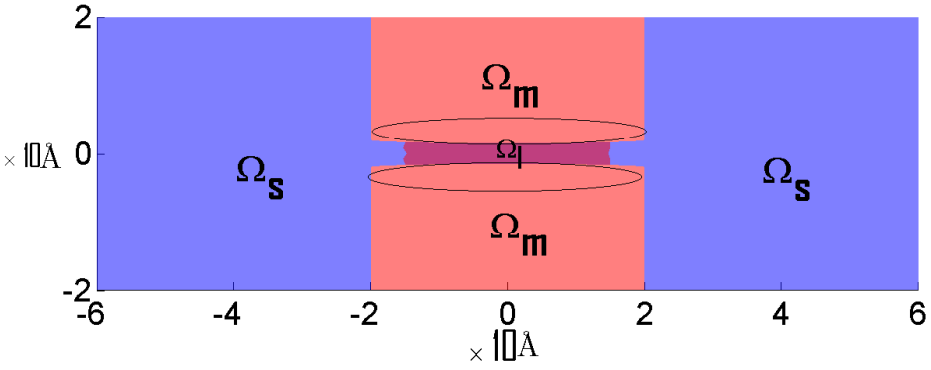

(b)

Fig. 1. (a) A schematic picture of a single gramicidin A pore embedded in lipid bilayers. (b) The profile of corresponding 2D computation domain set in our model for a single gramicidin A pore with lipid bilayers. The whole box Ω consists of the macromolecule part Ω_m and the solvent region Ω_s. In the macromolecule part Ω_m, the bilayers and gramicidin A are represented by two slabs and two ellipses, respectively. In the solvent region Ω_s, Ω_I represents the channel part.

functional. First, we observe the following kinematic conservation of charge densities

$$n_t + \nabla \cdot (nu_n) = 0, \tag{2}$$

$$p_t + \nabla \cdot (pu_p) = 0, \tag{3}$$

and the Gauss's law:

$$-\varepsilon \triangle \phi = ze(p - n). \tag{4}$$

Where n (p) is the density of negative (positive) ions; u_n (u_p) is the velocity of the negative (positive) ions; ϕ is electrical potential; ε is the dielectric coefficient; $e = 1.6 \times 10^{-19}$ C is the charge for one electron; z is the

valence number of the negative or positive ion. The total energy includes all the equilibrium physics in the system:

$$E^{total} = \int_{\Omega} \left[K_B T (n \ln \frac{n}{n_\infty} + p \ln \frac{p}{p_\infty}) + \frac{\varepsilon}{2} |\nabla \phi|^2 \right] d\vec{x}, \tag{5}$$

where $\vec{x}(t) = \vec{x}(\vec{X}, t)$ (with $\vec{x}(\vec{X}, 0) = \vec{X}$) is the flow map and $\vec{x} = (x, y)$ for the two dimensional case; n_∞ (p_∞) is the characteristic value of initial density of negative (positive) ions; K_B is the Boltzmann constant and T is the absolute temperature, $K_B T = 4.14 \times 10^{-21}$ J is the Boltzmann energy. The first and second terms are the thermal fluctuations (Gibbs entropy) of the ion species. The last term is the electro energy. The Gauss's law (4) is equivalent to

$$\phi(\vec{x}) = ze \frac{1}{\varepsilon} \int_{\Omega} G(\vec{x}, \vec{\xi})(n - p)(\vec{\xi}) d\vec{\xi}, \tag{6}$$

where $G(\vec{x}, \vec{\xi})$ is Green's kernel. By substituting (6) into (5), the energy can be written in the following nonlocal form [50]

$$E^{total} = \int_{\Omega} K_B T \left(n \ln \frac{n}{n_\infty} + p \ln \frac{p}{p_\infty} \right) d\vec{x} + \frac{ze}{2\varepsilon} \int_{\Omega} (p - n)(\vec{x}) \int_{\Omega} G(\vec{x}, \vec{\xi})(n - p)(\vec{\xi}) d\vec{\xi} d\vec{x}.$$

Above formula shows that the third term of total energy in fact is the Coulomb electro static interactions which is the particles interactions contributing to the internal energy $\mathcal{U}$. The dissipation functional is defined as follows, reflecting the linear response assumptions of the system,

$$\Delta = \int_{\Omega} K_B T \left[\frac{1}{D_n} n |u_n|^2 + \frac{1}{D_p} p |u_p|^2 \right] d\vec{x}. \tag{7}$$

In this case there are two flow maps corresponding to velocities fields, u_n and u_p : negative charge map $\vec{x}_n$ and positive charge map $\vec{x}_p$, respectively. Taking map $\vec{x}_n$ as example, by the Least Action Principle, we get the conservation force,

$$F_{n-con} = -\frac{\delta}{\delta x_n} E^{total} = -n \nabla \mu_n, \tag{8}$$

where $\mu_n := K_B T(1 + \ln n) - K_B T \ln n_\infty - ze\phi$ is the chemical potential for the negative charge.

Using the Maximum Dissipation Principle, we get the dissipation force,

$$F_{n-dis} = \frac{\delta}{\delta u_n} (\frac{1}{2} \Delta) = \frac{K_B T}{D_n} n u_n. \tag{9}$$

The total force balance equation yields:

$$n u_n = -\frac{D_n}{K_B T} n \nabla \mu_n. \tag{10}$$

Combining equation (10) and the mass conservation of negative charge (2), we obtain,

$$n_t = \nabla \cdot (D_n (\nabla n - \frac{ze}{K_B T} n \nabla \phi).$$

Similarly, for positive equation, we also have,

$$p u_p = -\frac{D_p}{K_B T} p \nabla \mu_p, \tag{11}$$

where $\mu_p := K_B T(1 + \ln p) - K_B T \ln n_\infty + ze\phi$ is the chemical potential of positive charge. Combining equation (11) and the mass conservation for the positive charge (3), we obtain,

$$p_t = \nabla \cdot \left(D_p \left(\nabla p + \frac{ze}{K_B T} p \nabla \phi \right) \right).$$

In summary, we obtain the coupled Poisson-Nernst-Planck system,

$$n_t = -\nabla \cdot J_n \quad \text{in } \Omega_s, \tag{12}$$

$$p_t = -\nabla \cdot J_p \quad \text{in } \Omega_s, \tag{13}$$

$$-\nabla \cdot (\varepsilon \nabla \phi) = (p - n)ze \quad \text{in } \Omega. \tag{14}$$

In the Nernst-Planck equations, (12) and (13), $J_n = -(D_n \nabla n - \frac{D_n ze}{K_B T} \nabla \phi n)$ and $J_p = -(D_p \nabla p + \frac{D_p ze}{K_B T} \nabla \phi p)$ are ion fluxes and in this paper we are working on two dimensional PNP equations on the x-y plane, which is a simplified model of the three dimensional. Outside the channel region, the diffusion constants are $D_p = 1.96 \times 10^{-9} m^2/s$, $D_n = 2.03 \times 10^{-9} m^2/s$ and they are $D_p/18$ and $D_n/18$ inside the channel [18, 45]; Ω_s is the solvent region, Ω is the simulation box. In the Poisson equation (14),

$$\varepsilon(\vec{x}) = \begin{cases} \varepsilon_m \varepsilon_0 & \vec{x} \in \Omega_m \\ \varepsilon_s \varepsilon_0 & \vec{x} \in \Omega_s \end{cases}, \tag{15}$$

where $\varepsilon_0 = 8.85 \times 10^{-12} C^2/(N \cdot m^2)$ is the dielectric constant of vacuum, $\varepsilon_m = 2$ is the relative dielectric constant of macromolecule, and $\varepsilon_s = 80$ is the relative dielectric constant of solvent. The valence number of the negative and positive ion z is equal to one in our model.

The boundary and initial conditions of the Poisson-Nernst-Planck equations are as follows,

$$\begin{cases} J_n \cdot \nu = J_p \cdot \nu = 0, & \text{on } \Gamma_1 \bigcup \Gamma_2; \\ n = n_\infty,\ p = p_\infty, & \text{on } \Gamma_3; \\ n(.,0) = n_\infty,\ p(.,0) = p_\infty, & \\ [\varepsilon \nabla \phi] \triangleq (\varepsilon_s \nabla \phi - \varepsilon_m \nabla \phi) \cdot \nu = \rho_{m_1}, & \text{on } \Gamma_1; \\ [\varepsilon \nabla \phi] = \rho_{m_2}, & \text{on } \Gamma_2; \\ \phi(x,t) = -\delta V x/L, & \text{on } \partial\Omega, \end{cases} \tag{16}$$

where ρ_{m_1} and ρ_{m_2} are the charge densities on the surface of membranes and protein, respectively. In particular, ρ_{m_2} is one part of the molecular structure (together with the geometric setting in the previous sections) of the gramicidin A protein. In these simulations, ρ_{m_1} and ρ_{m_2} have different values when the bilaryers and gramicidin A are charged due to enzymatic activity of PLD and due to the presence of charged group attachments, respectively. ν is unit normal vector with direction from solvent region to macromolecule part on the boundary. δV is the voltage difference between the left and right edges of the box along x direction. Since the gramicidin A pore is permeable to cations, the entrance of gramicidin A pore is located at the positively polarized side of membrane, more specifically, the entrance of gramicidin A is located at left (right) side of membrane when δV is positive (negative). L is the length of the box. The boundaries are shown in Fig. 2. The current in gramicidin A pore is defined as

$$I = e \int_{Ly} \left[D_n \frac{\partial n}{\partial x} - D_p \frac{\partial p}{\partial x} + \frac{D_p e}{K_B T} \frac{\partial \phi}{\partial x}(n + p) \right] dy, \tag{17}$$

where Ly is the slice of the channel along the y direction. It can be used in any x-position along the pore axis, and that shows only minor differences. Throughout this paper, we use the chord conductance of the gramicidin A pore. It is obtained by dividing the current by the corresponding voltage difference δV(300mV) added upon the boundaries of the computational domain.

Let $V_0 = \{v | v \in H^1(\Omega), v|_{\partial\Omega} = 0\}$ and $V_{0,\Gamma_3} = \{v \in H^1(\Omega_s), v|_{\partial\Gamma_3} = 0\}$. The weak forms of Poisson-Nernst-Planck equations are as follows: find $\phi \in L^2(0, T; V)$, $p,\ n \in L^2(0, T; V_{\Gamma_3}) \cap L^\infty(\Omega_T)$, such that

$$\int_\Omega \varepsilon \nabla \phi \nabla u d\vec{x} = \int_\Omega e(p - n) u d\vec{x} + \int_{\Gamma_1 \cup \Gamma_2} [\varepsilon \nabla \phi] u ds, \quad \text{for } \forall\, u \in V_0, \tag{18}$$

$$\int_{\Omega_s} \frac{\partial n}{\partial t} v d\vec{x} + \int_{\Omega_s} \left(D_n \nabla n - D_n \frac{e}{K_B T} n \nabla \phi \right) \cdot \nabla v d\vec{x} = 0, \quad \text{for } \forall\, v \in V_{0,\Gamma_3}, \tag{19}$$

$$\int_{\Omega_s} \frac{\partial p}{\partial t} v d\vec{x} + \int_{\Omega_s} \left(D_p \nabla p + D_p \frac{e}{K_B T} p \nabla \phi \right) \cdot \nabla v d\vec{x} = 0, \quad \text{for } \forall\, v \in V_{0,\Gamma_3}, \tag{20}$$

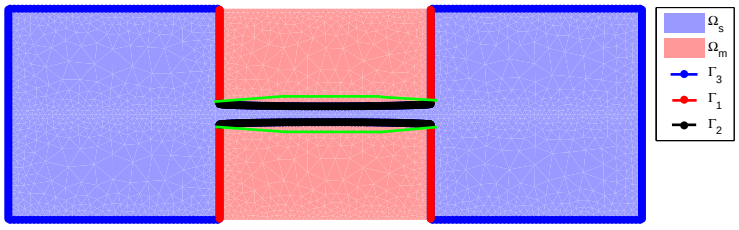

Fig. 2. The meshes of the simulation box and boundaries of Ω_s. The red lines, Γ_1, are the boundaries of membranes. The black lines, Γ_2, are the boundaries of protein exposed to solvent. The blue lines, Γ_3, are the outside boundaries of Ω_s.

where $V = \{v | v \in H^1(\Omega), v|_{\partial\Omega} = -\delta Vx/L\}$, $V_{\Gamma_3} = \{v \in H^1(\Omega_s), v|_{\partial\Gamma_3} = n_\infty\}$, and $\Omega_T = (0, T) \times \Omega$.

For the stability of solution with respect to the jump condition, we have the following lemma.

Lemma 2. 1. *Considering p_1, n_1, ϕ_1 and p_2, n_2, ϕ_2 are the solutions of Problem* (12)-(14) *with different jump condition $\rho_{m_1} = \sigma_1$ and $\rho_{m_1} = \sigma_2$, respectively. Here σ_1 and σ_2 are two constants. If $\phi_1(\phi_2) \in H^1(\Omega) \cap W^{1,\infty}(\Omega_s)$ and $p_1(p_2) \in H^1(\Omega_s) \cap L^\infty(\Omega_s)$, then there exists a constant such that*

$$\|p_1 - p_2\|_{L^2(\Omega_s)} + \|n_1 - n_2\|_{L^2(\Omega_s)} + \|\phi_1 - \phi_2\|_{H^1(\Omega)} \le C|\sigma_1 - \sigma_2|, \quad \text{for } 0 < t \le T.$$

Proof. If let $e_p = p_1 - p_2$, $e_n = n_1 - n_2$ and $e_\phi = \phi_1 - \phi_2$, then e_p, e_n and e_ϕ satisfy following problem

$$-\nabla \cdot (\varepsilon \nabla e_\phi) = (e_p - e_n)e \quad \text{in } \Omega. \tag{21}$$

$$\frac{\partial e_n}{\partial t} - \nabla \cdot (D_n \nabla e_n) = -\nabla \cdot (D_n \frac{e}{K_B T}(n_1 \nabla \phi_1 - n_2 \nabla \phi_2)) \quad \text{in } \Omega_s, \tag{22}$$

$$\frac{\partial e_p}{\partial t} - \nabla \cdot (D_p \nabla e_p) = \nabla \cdot (D_p \frac{e}{K_B T}(p_1 \nabla \phi_1 - p_2 \nabla \phi_2)) \quad \text{in } \Omega_s, \tag{23}$$

with initial and boundary values

$$\begin{cases} (\nabla e_n - \frac{e}{K_B T}(n_1 \nabla \phi_1 - n_2 \nabla \phi_2)) \cdot \nu = 0 & \text{on } \Gamma_1 \bigcup \Gamma_2; \\ (\nabla e_p + \frac{e}{K_B T}(p_1 \nabla \phi_1 - p_2 \nabla \phi_2)) \cdot \nu = 0, & \text{on } \Gamma_1 \bigcup \Gamma_2; \\ e_n = e_p = 0, & \text{on } \Gamma_3; \\ e_n(., 0) = e_p(., 0) = 0, & \\ [\varepsilon \nabla e_\phi] = (\sigma_1 - \sigma_2), & \text{on } \Gamma_1; \\ [\varepsilon \nabla e_\phi] = 0, & \text{on } \Gamma_2; \\ e_\phi = 0, & \text{on } \partial\Omega, \end{cases} \tag{24}$$

Multiplying (21) by e_ϕ and integrating by parts, we can obtain

$$\int_\Omega \varepsilon \nabla e_\phi \nabla e_\phi dx = e \int_{\Omega_s} (e_p - e_n) e_\phi dx + (\sigma_1 - \sigma_2) \int_{\Gamma_1} e_\phi ds. \tag{25}$$

By Hölder inequality, Poincaré inequality and trace theory, the above formula yields

$$\|\nabla e_\phi\|^2_{L^2(\Omega)} \le C(\|e_p - e_n\|_{L^2(\Omega_s)} \|e_\phi\|_{L^2(\Omega_s)} + |\sigma_1 - \sigma_2| \|e_\phi\|_{L^2(\Gamma_1)}) \tag{26}$$

$$\le C(\|e_p - e_n\|_{L^2(\Omega_s)} \|\nabla e_\phi\|_{L^2(\Omega)} + |\sigma_1 - \sigma_2| \|\nabla e_\phi\|_{L^2(\Omega)}) \tag{27}$$

$$\le C(\|e_p - e_n\|^2_{L^2(\Omega_s)} + |\sigma_1 - \sigma_2|^2) + \frac{1}{2} \|\nabla e_\phi\|^2_{L^2(\Omega)} \tag{28}$$

which means

$$\|\nabla e_\phi\|_{L^2(\Omega)} \le C(\|e_p - e_n\|_{L^2(\Omega_s)} + |\sigma_1 - \sigma_2|). \tag{29}$$

Multiplying (23) by e_p and integrating by parts, we get

$$\begin{aligned}
&\frac{1}{2}\frac{d}{dt}\|e_p\|^2_{L^2(\Omega_s)} + \lambda\|\nabla e_p\|^2_{L^2(\Omega_s)} \\
\leq\ & -\int_{\Omega_s} D_p \frac{e}{K_B T}(p_1\nabla\phi_1 - p_2\nabla\phi_2)\nabla e_p dx \\
\leq\ & -\int_{\Omega_s} D_p \frac{e}{K_B T}(e_p\nabla\phi_1 + p_2\nabla e_\phi)\nabla e_p \\
\leq\ & \Lambda\frac{e}{K_B T}\|e_p\|_{L^2(\Omega_s)}\|\nabla e_p\|_{L^2(\Omega_s)} + \Lambda\frac{e}{K_B T}\|\nabla e_\phi\|_{L^2(\Omega)}\|\nabla e_p\|_{L^2(\Omega_s)} \\
\leq\ & C(\|e_p\|^2_{L^2(\Omega_s)} + \|\nabla e_\phi\|^2_{L^2(\Omega)}) + \frac{\lambda}{2}\|\nabla e_p\|^2_{L^2(\Omega_s)},
\end{aligned} \tag{30}$$

where $\lambda = min_{x\in\Omega_s} D_p(x)$ and $\Lambda = max_{x\in\Omega_s} D_p(x)$. Here we have used the assumption $\nabla\phi_1 \in L^\infty(\Omega_s)$ and $p_2 \in L^\infty(\Omega_s)$. Combining with (29), the above formula yields

$$\begin{aligned}
\frac{d}{dt}\|e_p\|^2_{L^2(\Omega_s)} + \|\nabla e_p\|^2_{L^2(\Omega_s)} &\leq C(\|e_p\|^2_{L^2(\Omega_s)} + \|e_p - e_n\|^2_{L^2(\Omega_s)} + |\sigma_1 - \sigma_2|^2) \\
&\leq C(\|e_p\|^2_{L^2(\Omega_s)} + \|e_n\|^2_{L^2(\Omega_s)} + |\sigma_1 - \sigma_2|^2).
\end{aligned} \tag{31}$$

Similarly, we obtain

$$\frac{d}{dt}\|e_n\|^2_{L^2(\Omega_s)} + \|\nabla e_n\|^2_{L^2(\Omega_s)} \leq C(\|e_p\|^2_{L^2(\Omega_s)} + \|e_n\|^2_{L^2(\Omega_s)} + |\sigma_1 - \sigma_2|^2). \tag{32}$$

Adding (32) to (31), it gives

$$\frac{d}{dt}\left(\|e_p\|^2_{L^2(\Omega_s)} + \|e_n\|^2_{L^2(\Omega_s)}\right) \leq C(\|e_p\|^2_{L^2(\Omega_s)} + \|e_n\|^2_{L^2(\Omega_s)} + |\sigma_1 - \sigma_2|^2) \tag{33}$$

Using the Gronwall's inequality, we get

$$\|e_p\|^2_{L^2(\Omega_s)} + \|e_n\|^2_{L^2(\Omega_s)} \leq C(|\sigma_1 - \sigma_2|^2), \quad \text{for } 0 < t \leq T. \tag{34}$$

Combining with (29)and above formula, the lemma is proved. □

3 Numerical Simulation Schemes and Convergence Analysis

In this section, we present the numerical method applied for solving the Poisson-Nernst-Planck equations ((12), (13), (14)) and corresponding convergence theorem for the two dimensional case.

The finite element method is used to do the space discretization. For the charge distribution p and n, the piecewise linear element is used with the triangulation of domain Ω_s, $\mathcal{T}_h' = \{\tau_j'\}_{j=1}^{M_h^1}$. But for the potential, since the $\nabla\phi$ is the term we concerned in the charge distribution equations and the boundary Γ_2 is curved, the second order isoparametric finite element is used [9]. The triangulation of domain Ω, $\mathcal{T}_h = \{\tau_j\}_{j=1}^{M_h^2}$ is generated by a quadratic map based on the triangulation $\mathcal{T}_h'$. For a reference straight edge element $\hat{\tau}$ with node $\hat{a}_i$, $1 \leq i \leq 3$ and middle point of edge $\hat{a}_{ij}$, $1 \leq i < j \leq 3$, and an element τ in $\mathcal{T}_h$ with node a_i , $1 \leq i \leq 3$ and middle point of edge a_{ij}, $1 \leq i < j \leq 3$, there exists a quadratic map $F_\tau \in P_2(\hat{\tau})$, such that $F_\tau(\hat{a}_i) = a_i$ and $F_\tau(\hat{a}_{ij}) = a_{ij}$ [9]. In fact by the definition of F_τ, elements in $\mathcal{T}_h$ are straight edge triangles except the elements near the boundary Γ_2 where the quadratic curved edge triangles (Fig. 3) are used. If we let $\hat{P} = P_2(\hat{\tau})$ denote the second order polynomial in reference element $\hat{\tau}$, then we can define $P_\tau = \{p : p = \hat{p} \circ F_\tau^{-1}, \forall \hat{p} \in \hat{P}\}$ and isoparametric quadratic element space $S_2^h = \{v_h : v_h|_\tau \in P_\tau, \forall \tau \in \mathcal{T}_h\}$.

The finite element approximations to the weak forms of Poisson-Nernst-Planck equations (18) – (20) are that: find $n_h(\cdot, t)$, $p_h(\cdot, t) \in (n_\infty \bigoplus S^h_{0,\Gamma_3}(\Omega_s)) \cap V_{\Gamma_3}$, and $\phi_h(\cdot, t) \in (-\delta Vx \bigoplus S^h_{2,0}(\Omega)) \cap V$ for each $t > 0$, such

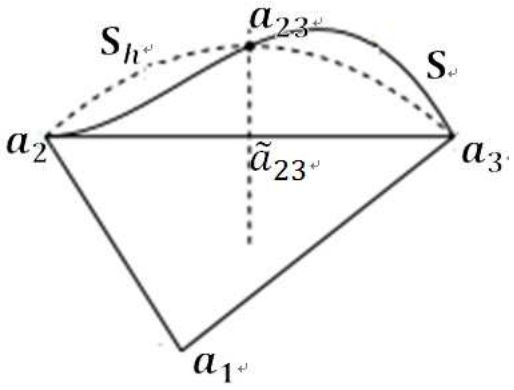

Fig. 3. The construction of the curved boundary triangle $a_1a_2a_3a_{23}$. Curved line S is the original boundary curve and dash line S_h is the approximated boundary curve. $\tilde{a}_{23} = (a_2 + a_3)/2$, a_{23} is on S and $\tilde{a}_{23}a_{23} \perp a_2a_3$. The curved edge S_h is a second order curve construed by the points a_2, a_3 and a_{23}.

that

$$\left\langle \frac{\partial p_h}{\partial t}, v_h \right\rangle_{\Omega_s} + \left\langle D_p \nabla p_h + \frac{D_p e}{K_B T} p_h \nabla \phi_h, \nabla v_h \right\rangle_{\Omega_s} = 0, \tag{35}$$

$$\left\langle \frac{\partial n_h}{\partial t}, v_h \right\rangle_{\Omega_s} + \left\langle D_n \nabla n_h - \frac{D_n e}{K_B T} n_h \nabla \phi_h, \nabla v_h \right\rangle_{\Omega_s} = 0, \tag{36}$$

$$\left\langle \varepsilon \nabla \phi_h, \nabla u_h \right\rangle_{\Omega} - \left\langle [\varepsilon \nabla \phi_h], u_h \right\rangle_{\Gamma_1 \cup \Gamma_2} - \left\langle (p_h - n_h)e, u_h \right\rangle_{\Omega_s} = 0, \tag{37}$$

for $\forall\, v_h \in S^h_{0,\Gamma_3}(\Omega_s)$ and $\forall\, u_h \in S^h_{2,0}(\Omega)$, where $S^h_{0,\Gamma_3}(\Omega_s) = \{\psi \in C(\Omega_s); \psi|_{\tau_j'} \in P_1; \psi|_{\partial\Gamma_3} = 0\}$ and $S^h_{2,0}(\Omega) = \{\psi \in S^h_2; \psi|_{\partial\Omega} = 0\}$. $\langle \cdot, \cdot \rangle_{\Omega}$ and $\langle \cdot, \cdot \rangle_{\Gamma}$ denote the L_2 inner product over the domain Ω and interface Γ, respectively.

If we define space $X = H^1(\Omega) \cap H^3(\Omega_s) \cap H^3(\Omega_m)$ equipped with the norm

$$\|v\|_X = \|v\|_{H^1(\Omega)} + \|v\|_{H^3(\Omega_s)} + \|v\|_{H^3(\Omega_m)}, \tag{38}$$

we can get the following convergence theorem.

Theorem 3. 2. *Let ϕ, p, n are the solutions of problem* (18)-(20) *and ϕ_h, p_h, n_h are the solutions of semi-discrete problem* (35)-(37). *If $\phi(\cdot, t) \in X \cap W^{1,\infty}(\Omega_s) \cap W^{1,\infty}(\Omega_m)$, $p(\cdot, t)$, $n(\cdot, t) \in H^2(\Omega_s) \cap L^\infty(\Omega_s)$, $\mathcal{T}_h$ and $\mathcal{T}_h'$ are quasiuniform, then*

$$\|\phi - \phi_h\|_{H^1(\Omega)} + \|p - p_h\|_{L^2(\Omega_s)} + \|n - n_h\|_{L^2(\Omega_s)} \le Ch^{3/2}, \quad \text{for } 0 < t \le T$$
$$\|\nabla(p - p_h)\|_{L^2(\Omega_s)} + \|\nabla(n - n_h)\|_{L^2(\Omega_s)} \le Ch^{1/2}, \quad \text{for } 0 < t \le T.$$

Before the proof of the theorem, we first present a prior regularity estimate of potential ϕ. The Poisson equation (14) is an elliptic equation with discontinuous coefficient. In Ref. [5], Babuska proved the regularity when the flux jump on the interface is zero. In Ref. [8], Chen and Zou presented a method to get the regularity when the flux jump is not zero by constructing an auxiliary function to cancel the jump. Here we use the similar method to get a higher estimate.

Lemma 3. 3. *Assume that $p,\ n \in H^1(\Omega_s)$. Then the Poisson equation* (14) *solution $\phi \in X$ satisfies a prior estimate*

$$\|\phi\|_X \le C(\|p - n\|_{H^1(\Omega_s)} + |\rho_{m_1}| + |\rho_{m_2}|). \tag{39}$$

Proof: We first let $v_1 \in H^1(\Omega_s)$ solve

$$\begin{cases} -\triangle v_1 + v_1 = 0, & \text{in } \Omega_s, \\ \varepsilon_s \frac{\partial v_1}{\partial \nu} = \rho_{m_1} & \text{on } \Gamma_1, \\ \varepsilon_s \frac{\partial v_1}{\partial \nu} = \rho_{m_2} & \text{on } \Gamma_2, \\ v_1 = 0, & \text{on } \partial\Omega \cap \partial\Omega_s. \end{cases}$$

We know that $v_1 \in H^3(\Omega_s)$ and $\|v_1\|_{H^3(\Omega_s)} \le C(|\rho_{m_1}| + |\rho_{m_2}|)$. Then we solve the following problem

$$\begin{cases} \triangle^2 v_2 = 0, & \text{in } \Omega_m, \\ v_2 = v_1,\ \varepsilon_m \frac{\partial v_2}{\partial \nu} = 0 & \text{on } \Gamma_1 \cup \Gamma_2, \\ v_2 = 0,\ \varepsilon_m \frac{\partial v_2}{\partial \nu} = 0 & \text{on } \partial\Omega \cap \partial\Omega_m. \end{cases}$$

Then we have

$$\|v_2\|_{H^3(\Omega_m)} \le C\|v_1\|_{H^{5/2}(\Gamma_1\cup\Gamma_2)} \le C\|v_1\|_{H^3(\Omega_s)} \le C(|\rho_{m_1}| + |\rho_{m_2}|). \tag{40}$$

If we define $\hat{v} = v_1$, in Ω_s and $\hat{v} = v_2$, in Ω_m, then $\hat{v} \in X$. We can set $\hat{\phi} = \phi - \hat{v}$, then

$$\begin{cases} -\nabla \cdot (\varepsilon \nabla \hat{\phi}) = (p - n)ze + \nabla \cdot (\varepsilon \nabla \hat{v}) & \text{in } \Omega. \\ \left[\hat{\phi}\right] = 0,\ \left[\varepsilon \nabla \hat{\phi}\right] = 0, & \text{on } \Gamma_1 \cup \Gamma_2 \\ \hat{\phi} = -\delta V x/L, & \text{on } \partial\Omega. \end{cases} \tag{41}$$

By the Theorem 1.1 in Babuska, [5] it yields

$$\|\hat{\phi}\|_X \le C(\|p - n\|_{H^1(\Omega_s)} + \|\hat{v}\|_X). \tag{42}$$

Then we have the estimate of ϕ

$$\|\phi\|_X \le (\|\hat{\phi}\|_X + \|\hat{v}\|_X) \le C(\|p - n\|_{H^1(\Omega_s)} + |\rho_{m_1}| + |\rho_{m_2}|). \quad \square \tag{43}$$

By a similar argument used in Ref. [8], we have the following lemma for the error estimate of the interpolation.

Lemma 3. 4. *([8]) If $v \in X$, $\mathcal{T}_h$ is quasiuniform and $\Pi_h : C(\bar{\Omega}) \mapsto S^h_{2,0}$ is the interpolation operator, then we have*

$$\|\Pi_h v - v\|_{L^2(\Omega)} + h\|\nabla(\Pi_h v - v)\|_{L^2(\Omega)} \le Ch^{5/2}(\ln h)^{1/2}\|v\|_X. \tag{44}$$

Furthermore, if $v \in W^{1,\infty}(\Omega_s) \cap W^{1,\infty}(\Omega_m)$, we have

$$\|\Pi_h v - v\|_{L^2(\Omega)} + h\|\nabla(\Pi_h v - v)\|_{L^2(\Omega)} \le Ch^{5/2}\|v\|_X. \tag{45}$$

In the following proof of the theorem, we take the the homogeneous Dirichlet boundary condition, i.e. $n_\infty = p_\infty = \delta V = 0$. For the general case, we obtain a similar proof by setting $\widetilde{p} = p - p_\infty$, $\widetilde{n} = n - n_\infty$, and $\widetilde{\phi} = \phi + \delta V x$.

Proof of Theorem 2. A traditional trick in nonlinear partial different equation analysis will be used. At first, we define a continuous cut off function g,

$$g(v) = \begin{cases} v, & \text{if } |v| <= 2M; \\ 2M, & \text{if } v > 2M; \\ -2M, & \text{if } v < -2M. \end{cases} \tag{46}$$

Since $p,\ n \in L^\infty(\Omega_s)$, if let $M = \sup_{x\in\Omega_s}\{|p(x)| + |n(x)|\}$, then $p \equiv g(p)$ and $n \equiv g(n)$. This means that (18)-(20) can be rewritten in the following forms,

$$\int_\Omega \varepsilon\nabla\phi\nabla u d\vec{x} = \int_\Omega e(p-n)ud\vec{x} + \int_{\Gamma_1\cup\Gamma_2}[\varepsilon\nabla\phi]uds, \tag{47}$$

$$\int_{\Omega_s}\frac{\partial n}{\partial t}vd\vec{x} + \int_{\Omega_s}\left(D_n\nabla n - D_n\frac{e}{K_BT}g(n)\nabla\phi\right)\cdot\nabla v d\vec{x} = 0, \tag{48}$$

$$\int_{\Omega_s}\frac{\partial p}{\partial t}vd\vec{x} + \int_{\Omega_s}\left(D_p\nabla p + D_p\frac{e}{K_BT}g(p)\nabla\phi\right)\cdot\nabla v d\vec{x} = 0. \tag{49}$$

The corresponding finite element solutions are to find: $\widetilde{n}_h, \widetilde{p}_h \in S^h_{0,\Gamma_3}(\Omega_s)\cap V_{\Gamma_3}$, and $\widetilde{\phi}_h \in S^h_{2,0}(\Omega)\cap V$, such that

$$\left\langle\frac{\partial\widetilde{p}_h}{\partial t}, v_h\right\rangle_{\Omega_s} + \left\langle D_p\nabla\widetilde{p}_h + \frac{D_pe}{K_BT}g(\widetilde{p}_h)\nabla\widetilde{\phi}_h, \nabla v_h\right\rangle_{\Omega_s} = 0, \tag{50}$$

$$\left\langle\frac{\partial\widetilde{n}_h}{\partial t}, v_h\right\rangle_{\Omega_s} + \left\langle D_n\nabla\widetilde{n}_h - \frac{D_ne}{K_BT}g(\widetilde{n}_h)\nabla\widetilde{\phi}_h, \nabla v_h\right\rangle_{\Omega_s} = 0, \tag{51}$$

$$\left\langle\varepsilon\nabla\widetilde{\phi}_h, \nabla u_h\right\rangle_\Omega - \left\langle[\varepsilon\nabla\widetilde{\phi}_h], u_h\right\rangle_{\Gamma_1\cup\Gamma_2} - \left\langle(\widetilde{p}_h - \widetilde{n}_h)e, u_h\right\rangle_{\Omega_s} = 0. \tag{52}$$

Step 1: estimate $\|\nabla(\phi - \widetilde{\phi}_h)\|_{L^2(\Omega)}$. Combining with the Lemma 4 and the fact that the isoparametric element makes the approximation error of the curved boundary Γ_2 up to h^3, following the method presented in Ref. [8], we get

$$\|\nabla(\widetilde{\phi}_h - \phi)\|_{L^2(\Omega)} \le C(h^{3/2} + \|\widetilde{p}_h - p\|_{L^2(\Omega_s)} + \|\widetilde{n}_h - n\|_{L^2(\Omega_s)}). \tag{53}$$

Step 2: estimate $\widetilde{p}_h - p$ and $\widetilde{n}_h - n$.

Set $\widetilde{p}_h - p = \theta + \rho$, where $\theta = \widetilde{p}_h - R_hp$, $\rho = R_hp - p$, R_hp is the Ritz projection and $(D_p\nabla R_hp, \nabla v_h)_{\Omega_s} = (D_p\nabla p, v_h)_{\Omega_s}$, for $v_h \in S^h_{0,\Gamma_3}(\Omega_s)$. By the Ritz projection operator estimate lemma in Ref. [44], it yields

$$\|\rho\|_{L^2(\Omega_s)} \le Ch^2\|p\|_{H^2(\Omega_s)},\ \|\rho_t\|_{L^2(\Omega_s)} \le Ch^2\|p_t\|_{H^2(\Omega_s)}. \tag{54}$$

In order to estimate θ, we note that by our definitions, for $v_h \in S^h_{0,\Gamma_3}(\Omega_s)$,

$$\begin{aligned}\left(\frac{\partial\theta}{\partial t}, v_h\right)_{\Omega_s} + (D_p\nabla\theta, \nabla v_h)_{\Omega_s} &= \left(\frac{\partial\widetilde{p}_h}{\partial t}, v_h\right)_{\Omega_s} + \left(D_p\nabla\widetilde{p}_h, \nabla v_h\right)_{\Omega_s} - \left(\frac{\partial R\widetilde{p}_h}{\partial t}, v_h\right)_{\Omega_s} + (D_p\nabla R\widetilde{p}_h, \nabla v_h)_{\Omega_s}\\ &= -\left(D_p\frac{e}{K_BT}g(\widetilde{p}_h)\nabla\widetilde{\phi}_h, \nabla v_h\right)_{\Omega_s} - \left(\frac{\partial R\widetilde{p}_h}{\partial t}, v_h\right)_{\Omega_s} + (D_p\nabla p, \nabla v_h)_{\Omega_s}\\ &= \left(\frac{\partial\rho}{\partial t}, v_h\right)_{\Omega_s} + \frac{e}{K_BT}\left(D_p(g(p)\nabla\phi - g(\widetilde{p}_h)\nabla\widetilde{\phi}_h), \nabla v_h\right)_{\Omega_s}.\end{aligned} \tag{55}$$

By setting $v_h = \theta$ and $\lambda = minD_p$, the above formula implies

$$\begin{aligned}&\frac{1}{2}\frac{d}{dt}\|\theta\|^2_{L^2(\Omega_s)} + \lambda\|\nabla\theta\|^2_{L^2(\Omega_s)}\\ \le\ &\|\rho_t\|_{L^2(\Omega_s)}\|\theta\|_{L^2(\Omega_s)} + \frac{e}{K_BT}\left(D_p(g(p)\nabla\phi - g(\widetilde{p}_h)\nabla\widetilde{\phi}_h), \nabla\theta\right)_{\Omega_s}\\ \le\ &\|\rho_t\|_{L^2(\Omega_s)}\|\theta\|_{L^2(\Omega_s)} + \frac{e}{K_BT}\left((D_p(g(p) - g(\widetilde{p}_h))\nabla\phi, \nabla\theta)_{\Omega_s} + (D_p\widetilde{p}_h\nabla(\phi - \widetilde{\phi}_h), \nabla\theta)_{\Omega_s}\right)\\ \le\ &\|\rho_t\|_{L^2(\Omega_s)}\|\theta\|_{L^2(\Omega_s)} + C(\|p - \widetilde{p}_h\|_{L^2(\Omega_s)} + \|\nabla(\phi - \widetilde{\phi}_h)\|_{L^2(\Omega_s)})\|\nabla\theta\|_{L^2(\Omega_s)}.\end{aligned}$$

Here we use the fact $\|g(u) - g(v)\|_{L^2(\Omega_s)} \le \|u - v\|_{L^2(\Omega_s)}$ for $u,\ v \in L^2(\Omega_s)$ and $g(p_h)$ is bounded by the definition of function g. Using the estimate (53), Poincaré inequality and the Hölder inequality, we have the estimate

$$\begin{aligned}\frac{1}{2}\frac{d}{dt}\|\theta\|^2_{L^2(\Omega_s)} + \lambda\|\nabla\theta\|^2_{L^2(\Omega_s)} &\le \|\rho_t\|_{L^2(\Omega_s)}\|\theta\|_{L^2(\Omega_s)} + C(h^{3/2} + \|p - \widetilde{p}_h\|_{L^2(\Omega_s)} + \|n - \widetilde{n}_h\|_{\Omega_s})\|\nabla\theta\|_{L^2(\Omega_s)}\\ &\le C(\|\rho_t\|^2_{L^2(\Omega_s)} + h^3 + \|p - \widetilde{p}_h\|^2_{L^2(\Omega_s)} + \|n - \widetilde{n}_h\|^2_{L^2(\Omega_s)}) + \frac{\lambda}{2}\|\nabla\theta\|^2_{L^2(\Omega_s)}\\ &\le C(h^4\|p_t\|^2_{L^2(\Omega_s)} + h^3 + \|p - \widetilde{p}_h\|^2_{L^2(\Omega_s)} + \|n - \widetilde{n}_h\|^2_{L^2(\Omega_s)}) + \frac{\lambda}{2}\|\nabla\theta\|^2_{L^2(\Omega_s)}.\end{aligned}$$

Here we use the inequality $\|\rho_t\|_{L^2(\Omega_s)} \le Ch^2\|p_t\|_{L^2(\Omega_s)}$. Considering $\|\nabla\theta\|^2_{L^2(\Omega_s)} \ge 0$, above formula gives

$$\frac{1}{2}\frac{d}{dt}\|\theta\|^2_{L^2(\Omega_s)} \le C(h^3 + \|p-\widetilde{p}_h\|^2_{L^2(\Omega_s)} + \|n-\widetilde{n}_h\|^2_{L^2(\Omega_s)}). \tag{56}$$

Combining with the estimate of ρ and ρ_t, we derive

$$\frac{1}{2}\frac{d}{dt}\|\widetilde{p}_h - p\|^2_{L^2(\Omega_s)} \le C(h^3 + \|p-\widetilde{p}_h\|^2_{L^2(\Omega_s)} + \|n-\widetilde{n}_h\|^2_{L^2(\Omega_s)}). \tag{57}$$

Similarly for $\widetilde{n}_h - n$, we have

$$\frac{1}{2}\frac{d}{dt}\|\widetilde{n}_h - n\|^2_{L^2(\Omega_s)} \le C(h^3 + \|p-\widetilde{p}_h\|^2_{L^2(\Omega_s)} + \|n-\widetilde{n}_h\|^2_{L^2(\Omega_s)}). \tag{58}$$

Adding (58) with (57), we have

$$\frac{1}{2}\frac{d}{dt}\left(\|\widetilde{p}_h - p\|^2_{L^2(\Omega_s)} + \|\widetilde{n}_h - n\|^2_{L^2(\Omega_s)}\right) \le C(h^3 + \|p-\widetilde{p}_h\|^2_{L^2(\Omega_s)} + \|n-\widetilde{n}_h\|^2_{L^2(\Omega_s)}) \tag{59}$$

Then by using the Gronwall's inequality, we obtain

$$\|\widetilde{p}_h - p\|^2_{L^2(\Omega_s)} + \|\widetilde{n}_h - n\|^2_{L^2(\Omega_s)} \le Ch^3, \text{ for } 0 < t < T. \tag{60}$$

By using the inverse inequality, above formula deduces

$$\|\widetilde{p}_h - p\|_{L^\infty(\Omega_s)} + \|\widetilde{n}_h - n\|_{L^\infty(\Omega_s)} \le Ch^{1/2}, \text{ for } 0 < t < T. \tag{61}$$

Estimate (61) means that $\sup|\widetilde{p}_h| \le 2M$, $\sup|\widetilde{n}_h| \le 2M$ for sufficiently small $h > 0$, i.e. $g(\widetilde{p}_h) \equiv \widetilde{p}_h$ and $g(\widetilde{n}_h) \equiv \widetilde{n}_h$. Comparing the formula (50)-(52) with (35)-(37), we get $\phi_h = \widetilde{\phi}_h$, $p_h = \widetilde{p}_h$ and $n_h = \widetilde{n}_h$. Then, combining with (53) and (60) and replacing $\widetilde{\phi}_h$, $\widetilde{p}_h$, $\widetilde{n}_h$ by ϕ_h, p_h, n_h, respectively, we can obtain,

$$\|\phi - \phi_h\|_{H^1(\Omega)} + \|p - p_h\|_{L^2(\Omega_s)} + \|n - n_h\|_{L^2(\Omega_s)} \le Ch^{3/2}. \tag{62}$$

Using the inverse inequality, we have

$$\|\nabla(p - p_h)\|_{L^2(\Omega_s)} + \|\nabla(n - n_h)\|_{L^2(\Omega_s)} \le Ch^{1/2}, \quad \text{for } 0 < t \le T. \tag{63}$$

□

The implicit Euler scheme is used to do the time discretization with time step Δt. To solve the coupled system ((35), (36) and (37)) at each time step, the convex iteration [15, 16, 31] is employed as follows.

- step 1: Let $m = 1$, and $p_h^{k_m} = p_h^k$, $n_h^{k_m} = n_h^k$, $\phi_h^{k_m} = \phi_h^k$.
- step 2: solve the following equations for $n_h^{k_{m+1}}$, $p_h^{k_{m+1}}$, with given $n_h^{k_m}$, $p_h^{k_m}$ and $\phi_h^{k_m}$ using Edge Average Finite Element method (EAFEM) [49].

$$\begin{aligned}
\left\langle \frac{p_h^{k_{m+1}} - p_h^{k_m}}{\Delta t}, v_h \right\rangle_{\Omega_s} + \left\langle D_p \nabla p_h^{k_{m+1}} + \frac{D_p e}{K_B T} p_h^{k_{m+1}} \nabla \phi_h^{k_m}, \nabla v_h \right\rangle_{\Omega_s} &= 0, \\
\left\langle \frac{n_h^{k_{m+1}} - n_h^{k_m}}{\Delta t}, v_h \right\rangle_{\Omega_s} + \left\langle D_n \nabla n_h^{k_{m+1}} - \frac{D_n e}{K_B T} n_h^{k_{m+1}} \nabla \phi_h^{k_m}, \nabla v_h \right\rangle_{\Omega_s} &= 0.
\end{aligned}$$

- step 3: Let $p_h^{k_{m+1}} = cp_h^{k_{m+1}} + (1-c)p_h^{k_m}$, $n_h^{k_{m+1}} = cn_h^{k_{m+1}} + (1-c)n_h^{k_m}$, $0 < c \le 1$ and solve Poisson equation

$$\left\langle \varepsilon \nabla \phi_h^{k_{m+1}}, \nabla u_h \right\rangle_\Omega - \left\langle [\varepsilon \nabla \phi^{k_{m+1}}], u_h \right\rangle_{\Gamma_1 \cup \Gamma_2} - \left\langle (p_h^{k_{m+1}} - n_h^{k_{m+1}})e, u_h \right\rangle_\Omega = 0$$

  and then update $\phi^{k_{m+1}} = c\phi^{k_{m+1}} + (1-c)\phi^{k_m}$.

- step 4: if $n_h^{k_{m+1}}$, $p_h^{k_{m+1}}$, $\phi_h^{k_{m+1}}$ are closed to $n_h^{k_m}$, $p_h^{k_m}$, $\phi_h^{k_m}$, then update $n_h^{k+1} = n_h^{k_{m+1}}$, $p_h^{k+1} = p_h^{k_{m+1}}$, $\phi_h^{k+1} = \phi_h^{k_{m+1}}$ and stop. Otherwise let $m = m + 1$ and go to step 2.

In the practical simulations of this ion channel system with the high jump conditions, if we start the convex iteration directly from a trivial charge density, such as $p = p_\infty$ and $n = n_\infty$, this will cost a very long iteration process to get the convergent steady state. With the Lemma 1, we know that the steady state solution is continuous with respect to the jump conditions. This provides us an iteration strategy for accelerating this convergent process to steady state. That is we do the continuation of the steady state solution with respect to the jump conditions, i.e. the steady state solutions of the PNP with low jump conditions are used as the initial densities for PNP system with a little higher jump condition. Lemma 1 ensures that as long as the change in the jump condition is small, the change of the steady solution is also small. Thus it is easy to get the steady solution with the initial density is the steady solution with a closed jump condition. So, in practical simulation, we start the time evolving from the low jump conditions, then increase the jump conditions a little bit whenever the system reaches equilibrium until we have the steady solution with the high jump conditions. This strategy can also be adopt in solving the steady state PNP directly.

In these simulations, we use a widely used meshing tool, Distmesh [35], to generate the triangular meshes conforming the interface Γ of the box Ω. The mesh used here is refined near the boundary to seize the behavior of boundary layer and save the computational cost. The programme is under the frame work of iFEM toolbox (https://bitbucket.org/ifem/ifem).

4 Results of Numerical Simulations

To demonstrate the conductance changes of gramicidin A pore in the presence of electrical charges on the surface of membrane, the I-V curves with different positive applied voltages (δV) are plotted in Fig. 5, and the conductances with negative charge densities on each side of the bilayer are shown in Fig. 6 (the positions of negative charges are illustrated in Fig. 4). Here the applied voltages (δV) are positive, as stated in Section 2.2, the entrance of pore is on the left side of the membrane In these simulations, the negative charge density on the surface of channel, ρ_{m_2} is $-10 \times 0.0013e/\text{Å}^2$. We got this value through fitting the numerical result of this model to the experimental result of the conductance. As shown in Fig. 5 and 6, the current and the conductance of gramicidin A increase dramatically only when the magnitude of the negative charge densities increase on the left leaflet of the membrane where the entrance of the channel is located. Both current and conductance almost remains constant as the magnitude of the negative charge densities increase on right leaflet of the membrane where the exit of the channel is located. Moreover, gramicidin A conductance increases almost linearly when the magnitude of the negative charge densities on the left side of the lipid bilayer is smaller than $4 \times 0.0013e/\text{Å}^2$, and reaches saturation when the magnitude of the negative charge density on the bilayer becomes larger than $10 \times 0.0013e/\text{Å}^2$. These simulation results are in good qualitatively agreement with the experimental results reported by Majd et al. [28].

The steady-state ion concentrations and electric potentials for these cases along the central line of the solvent box ($y = 0$) with the same applied voltage are shown in Fig. 7 and Fig. 8. Fig. 7 shows that the concentration of positive charge is much higher than that of negative charge in the pore (-20 Å $< x <$ 20 Å). This is in agreement with the fact that gramicidin A pores are permeable to cations. It is also shown in Fig. 7 that in the channel region (-20 Å $< x <$ 20 Å) the positive and negative charge densities are almost the same when the different sides of bilayer are negatively charged. Fig. 8 demonstrates that the slop of electrical potential increases as more negative charges are added to the left side of the bilayer, while the potential almost remains the same as more negative charges are added to the right side of bilayer. Together with the definition of current in the channel in (17), we can see that the current passing through the pore is more affected by the electrical potential than by the charge densities within the pore.

It is also illustrated in Fig. 9 that the positive charges are attracted by the negatively charged lipid surface and accumulate to high densities near the negatively charged side of the bilayer, and the negative charges are repelled by the negatively charged lipid surface, as expected.

The above results suggest that the negative charges near the entrance of the gramicidin A pore (the positively polarized compartment of the bilayer) have much more effect on the conductance of the channel than

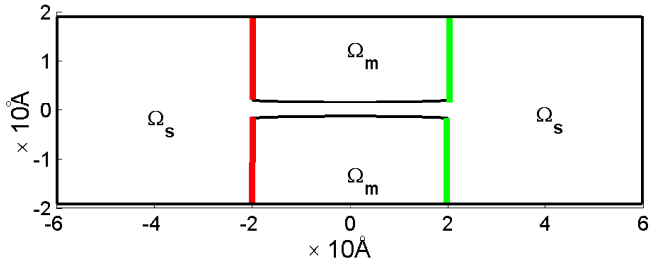

Fig. 4. Negative charges are placed on the left side of bilayer (red) and the right side of bilayer (green), respectively.

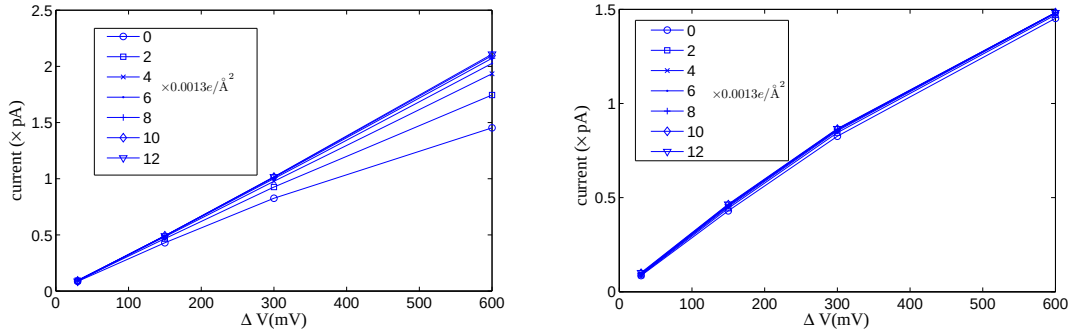

(a) **(b)**

Fig. 5. The IV curves with different amounts of negative charge present on (a) the left side of bilayer (the pore entrance located side) and (b) the right side (the pore exit located side) of bilayer.

those far from the entrance of the gramicidin A pore. To examine this, we performed the numerical simulations with the following two different negative charges distributions on the left side (positively polarized) of bilayer. One places the negative charges on left side of membrane far from the entrance of pore, $\Gamma^l_{far} = \Gamma_1 \cap \{x = -20\ \text{Å}, |y| > 10\ \text{Å}\}$, while the other places negative charges on side of the membrane near the entrance of pore, $\Gamma^l_{near} = \Gamma_1 \cap \{x = -20\ \text{Å}, |y| < 10\ \text{Å}\}$, i.e.

$$\rho_{m_1} = \begin{cases} \rho_0 \times 0.0013e/\text{Å}^2, & \text{on } \Gamma^l_{far} \\ 0, & \text{otherwise} \end{cases}, \tag{64}$$

and

$$\rho_{m_1} = \begin{cases} \rho_0 \times 0.0013e/\text{Å}^2, & \text{on } \Gamma^l_{near} \\ 0, & \text{otherwise} \end{cases}, \tag{65}$$

where $\rho_0 = -2k,\ k = 0, 1, \cdots, 11$ in the simulation. Fig. 10 illustrates the locations of Γ^l_{near} and Γ^l_{far}. Here, the applied voltages are set to be positive, thus the entrance and exit of the pore are located at left and right of the membrane, respectively. Similarly, the places on the right side of membrane near and far from the exit of the pore are defined as $\Gamma^r_{near} = \Gamma_1 \cap \{x = 20\ \text{Å}, |y| < 10\ \text{Å}\}$ and $\Gamma^r_{far} = \Gamma_1 \cap \{x = 20\ \text{Å}, |y| > 10\ \text{Å}\}$, respectively. The conductances of gramicidin A pore with different amounts of negative charge placed on Γ^r_{far} and Γ^r_{near} are also simulated. The results are shown in Fig. 11.

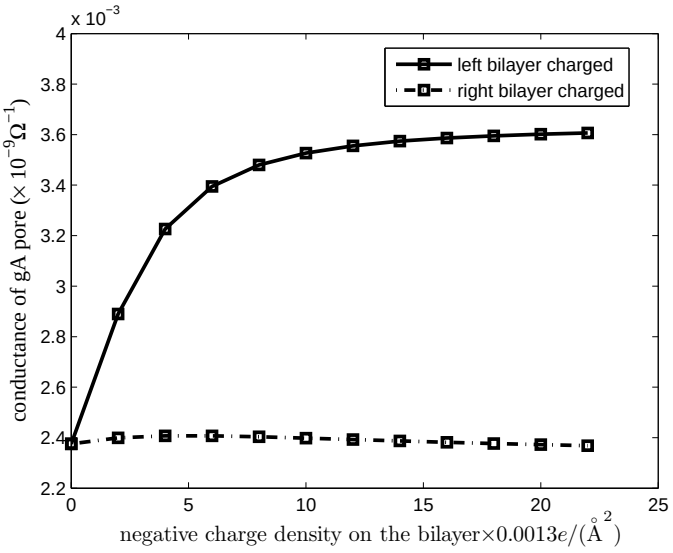

Fig. 6. The changes in the conductance of gramicidin A channel as a function of amount of negative charges present on right (dashed lines, the pore exit located side) and left (solid lines, the pore entrance located side) side of the bilayer.

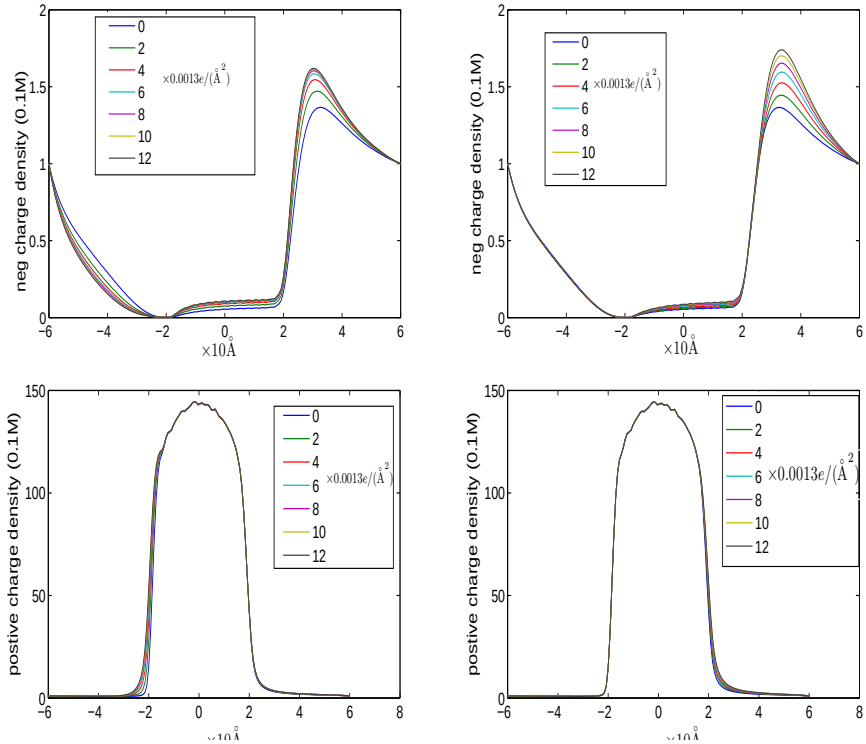

Fig. 7. Distributions of negative charges (first row) and positive charges (second row) along the central line of the solvent box (y=0) when different side of the bilayer is negatively charged. The left and right columns correspond to the charged side of membrane (i.e., left and right side, respectively).

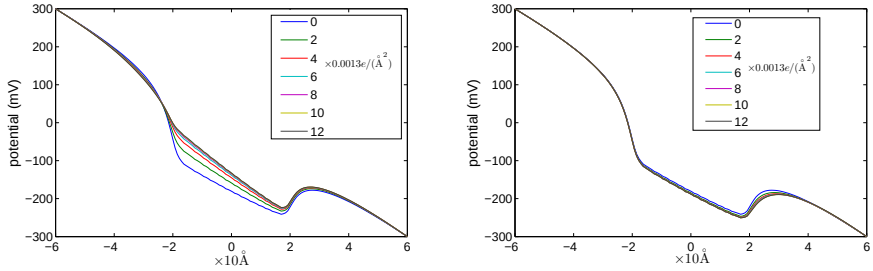

Fig. 8. Electrical potentials along the central line of the solvent box (y=0) when different side of membrane is negatively charged. The left and right columns correspond to the charged side of membrane (i.e., left (the pore entrance located side) and right side (the pore exit located side), respectively).

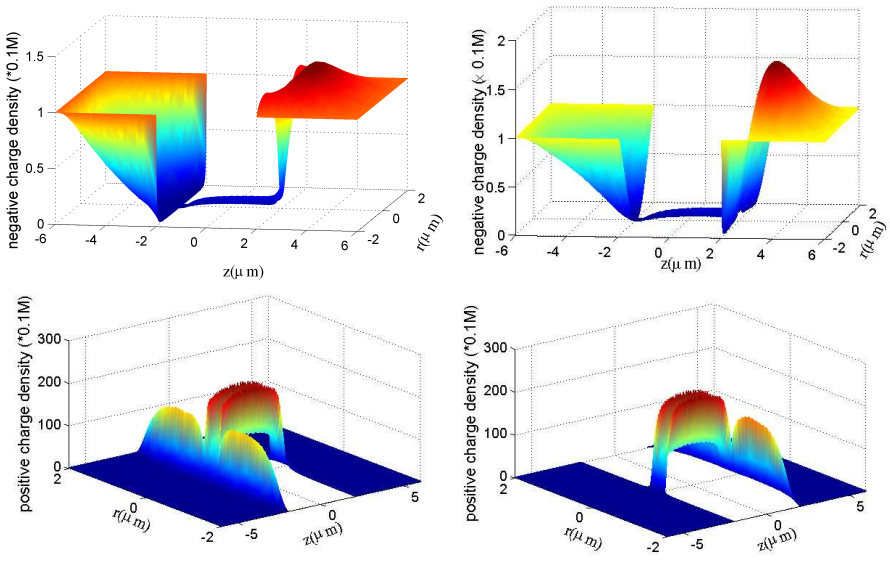

Fig. 9. Distributions of negative charges (first row), positive charges (second row) in the solvent region when different sides of lipid bilayer bears negative charges. The left and right columns correspond to the situations where the left and the right sides of lipid bilayers are charged, respectively.

Interestingly, Fig. 11 demonstrates that the amplitudes of the conductances are smaller and the asymmetrical effect becomes a little insignificant when the negative charges are placed far away from the channel. Here, the asymmetrical effect is the difference between the curves of conductances corresponding to two different cases, one is changing the surface charges near the entrance of the pore the other is the surface charges near the exit of the pore. The difference between slopes of curves is one of the quantifications of the asymmetrical effect. This result highlights the importance of the location of charged species with respect to the gramicidin A entrance.

Furthermore, to study the relationship between the conductance and the width of the pore, the changes of conductance as a function of pore width are simulated. Fig. 12 displays the results of these simulations. It can be seen that the asymmetrical effect is less pronounced when the pore opens wider. This result emphasizes the importance of the size of the channel opening for sensing purposes. Extremely small width of gramicidin A channel makes this peptide an attractive choice for biochemical sensing applications.

Moreover, to extend this model to predict gramicidin A conductance in the presence of charges associated on the protein surface inside the pore, we simulated the conductance changes with different negative charge densities ρ_{m_2} on Γ_2. Fig. 13 shows that smaller magnitude of negative charge density on the gramicidin A surface exposed to solvent causes the conductance to reach a lower saturation. This result also demonstrates

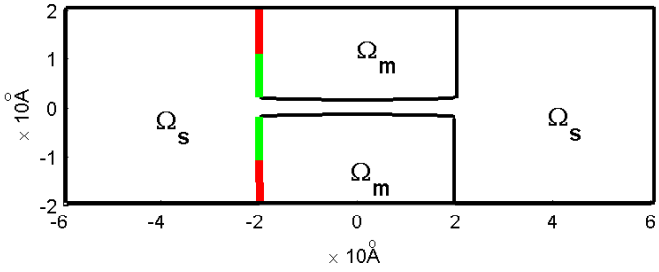

Fig. 10. Negative charges are placed near the entrance (Γ^l_{far}, green) and far away from the entrance (Γ^l_{near}, red), respectively.

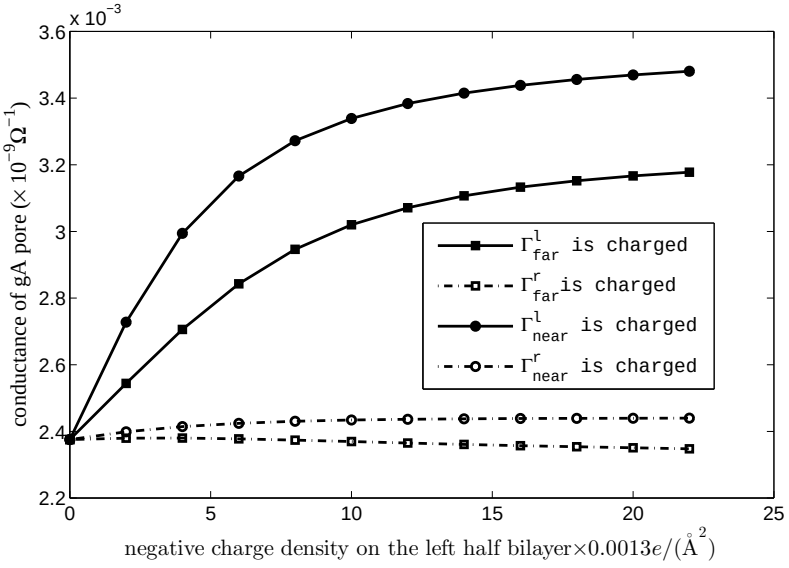

Fig. 11. The changes of conductances of the gramicidin A pore as the bilayer surface near (Γ^l_{near} and Γ^r_{near}, circles) or far away (Γ^l_{far} and Γ^r_{far}, rectangles) from the pore is negatively charged. Solid and dashed curves correspond to the negatively charged left (pore entrance located) and right (pore exit located) sides of the bilayer, respectively.

that the sensitivity of gramicidin A conductance to the local environments strongly depends on the magnitude of the surface charge densities inside the pore.

We also simulated the cases of that the current and conductance changes led by the different modified charged attachments at the tails of gramicidin As (C-terminers of gramicidin A). In these simulations, the current and conductance of native gramicidin A channel are compared with those of the following three cases. The first is the modified negatively charged tails (gA-T$^-$), in this case,

$$\rho_{m_2} = \begin{cases} -20 \times 0.0013e/\text{Å}^2, & on\ \{40/3\ \text{Å} < |x| \le 20\ \text{Å}\} \cap \Gamma_2 \\ -10 \times 0.0013e/\text{Å}^2, & on\ \{|x| \le 40/3\ \text{Å}\} \cap \Gamma_2 \end{cases}, \tag{66}$$

The second is trimethylgramicidine A channel with positive charged tails (gA-NMe$_3^+$). In this situation, we set

$$\rho_{m_2} = \begin{cases} 5 \times 0.0013e/\text{Å}^2, & on\ \{40/3\text{Å} < |x| \le 20\ \text{Å}\} \cap \Gamma_2 \\ -10 \times 0.0013e/\text{Å}^2, & on\ \{|x| \le 40/3\text{Å}\} \cap \Gamma_2 \end{cases}.$$

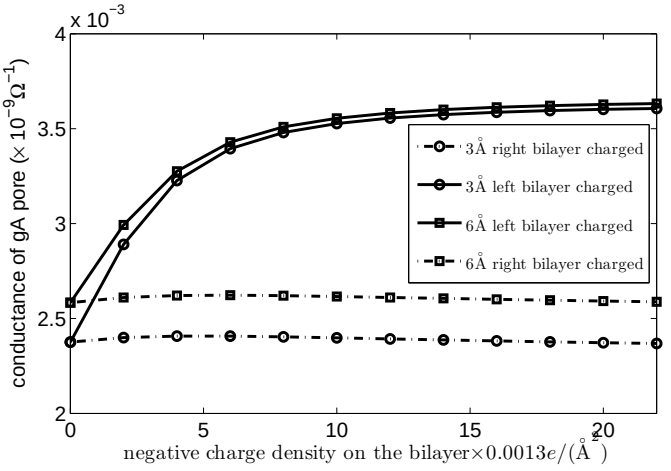

Fig. 12. The changes of conductances of the gramicidin A pores having two different widths as the negative charges accumulating at the different sides of bilayer. The circles and rectangles show the cases that widths at the centers of the pores are 6 Å and 3 Å, respectively. Solid and dashed curves correspond to the negatively charged left (pore entrance located) and right (pore exit located) sides of the bilayer, respectively.

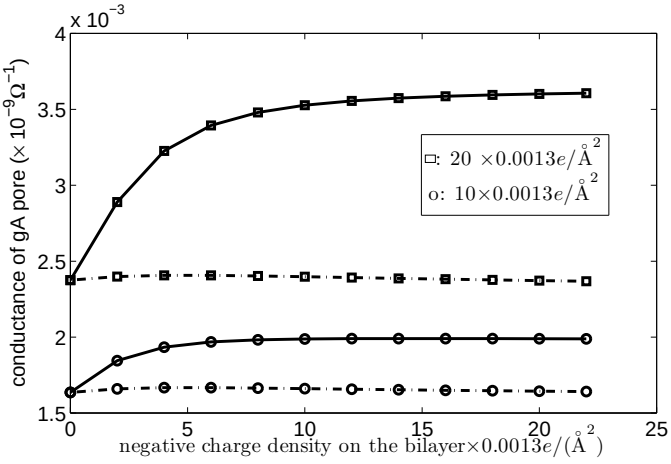

Fig. 13. The changes of conductances of the gramicidin A pore with different negative charge densities on gramicidin A surface exposed to solvent, Γ_2. The circles and rectangles show the cases in which $\rho_{m_2} = -10 \times 0.0013e/\text{Å}^2$ (circles) and $\rho_{m_2} = -20 \times 0.0013e/\text{Å}^2$ (rectangles) on Γ_2. The solid and dashed curves correspond to the negatively charged side of membrane (i.e. the pore entrance and pore exit located sides), respectively.

In the third case, the channel is formed by two different modified gramicidin A monomers, gA-T$^-$ and gA-NMe$_3^+$, and the charge density on Γ_2 is set as

$$\rho_{m_2} = \begin{cases} -20 \times 0.0013e/\text{Å}^2, & on\ \{-20\ \text{Å} < x \le -40/3\ \text{Å}\} \cap \Gamma_2 \\ -10 \times 0.0013e/\text{Å}^2, & on\ \{|x| \le 40/3\ \text{Å}\} \cap \Gamma_2 \\ 5 \times 0.0013e/\text{Å}^2, & on\ \{40/3\ \text{Å} < x \le 20\ \text{Å}\} \cap \Gamma_2 \end{cases} .$$

Fig. 14 illustrates the locations of different charges added to the surface near the tails of Gramicidin As.

According to the experimental results reported in references [25–27], it is expected in the numerical results that the current and conductance change symmetrically with respect to the polarity of the applied voltages in the first and second cases, while they change asymmetrically in the third case. As shown in Fig. 15, the gramicidin A conductance is significantly influenced by the charges attached to the tails of gramicidin A monomers. when the gramicidin A tails are both negatively charged (gA-T$^-$), the current and conductance increase compared with the case of native gramicidin A. The gramicidin A current and conductance decrease

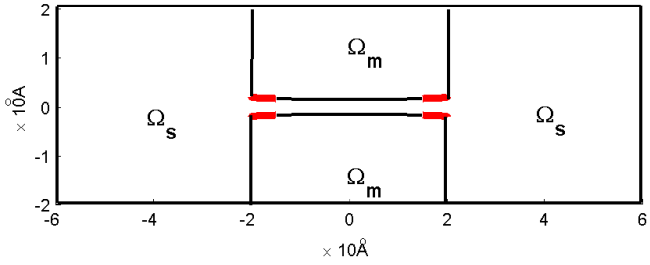

Fig. 14. The locations (red lines) of surface charges added by the modified groups at the tails of gramicidin As.

when positively charged chemical groups (NMe_3^+) are attached to the tails of gramicidin A monomers. As shown in Fig. 16, when the tails are modified by different charged groups (left and right tails are charged negatively and positively respectively), the asymmetrical current and conductance changes are also reproduced by our simulations. These findings are in excellent agreement with the experimental results reported by Yang and colleagues [25–27].

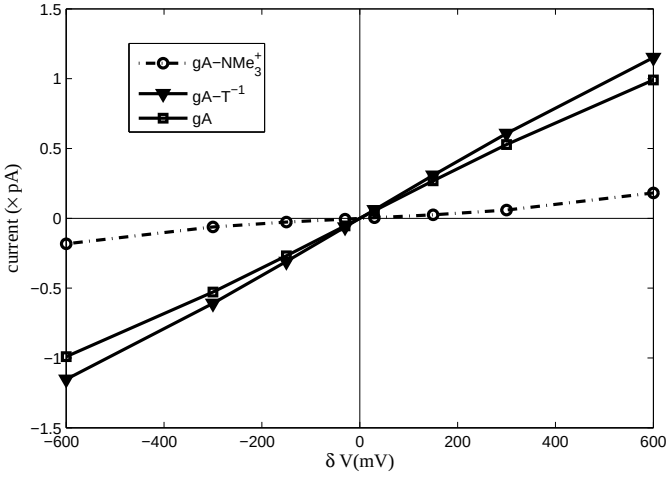

Fig. 15. The IV curves of the native gramicidin A and the cases of that different modified charged groups attach the both tails of gramicidin As.

5 Conclusions

In this study, we present a simplified mathematical/physical model for the asymmetrical conductance of the gramicidin A pore when there are electrical charges present around the channel, either on the membrane or attached to gramicidin A. This model is based on the Poisson-Nernst-Planck equations that are well established for describing the ion transport under the gradients of concentration and the electric field. Using

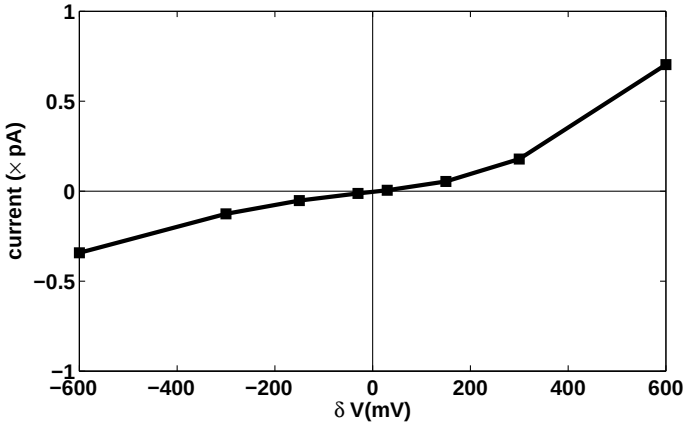

Fig. 16. The IV curves in the case of that different modified charged groups attach the tails of gramicidin As (left and right tails are charged negatively and positively, respectively).

finite element method to numerically solve the Poisson-Nernst-Planck equations on a simple two dimensional solvent domain, previously reported experimental results of asymmetrical changes in gramicidin A conductance are qualitatively reproduced. The simulation results also revealed that the gradient of electric field plays a critical role in gramicidin A asymmetrical behavior, and the conductance of the gramicidin A pore is more influenced by the presence of negative charges near the entrance of the pore than those far from the entrance.

As with gramicidin A channel, there are relatively few theoretical studies for conductance changes. In a previous work [7], Cardenas et al. simulated the effects on membrane gramicidin A electrostatics to the conductance based on the Poisson-Nernst-Planck model. The present work differs from work of Cardenas et al. in the following three aspects. Firstly, we address the specific issues of asymmetrical conductance changes and their relations to different parameters in the Poisson-Nernst-Planck model, such as the negative charge densities, and width of the pore, while the work by Cardenas mainly considered the effects of surface charges and dipoles in membrane on ion permeation through the gramicidin A pore. Secondly, compared with the uniformly lattice methodology used in Cardenas's work, EAFEM with unstructured meshes is adopted in our model for solving the Poisson-Nernst-Planck system. The EAFEM is more suitable for capturing the behavior of boundary layers on the interface between solvent and macromolecule in reaction-diffusion processes. Thirdly, the 3D structure of gramicidin A and bilayer are represented by lattices in Cardenas' paper, while in our simulations, we only modeled the structures of the channel system using 2D geometries of rectangles and ellipses and our corresponding 3D codes are under development. Although the 2D model used in our model is less realistic than 3D models, the essential asymmetrical effects are qualitatively reproduced by our model. This also suggests that the asymmetrical conductance change is a robust mechanism, insensitive to the exact three dimensional geometry structure of the channel. Additionally, the 2D model makes the computations less complicated and easier to be implemented. In the future, we will further implement the 3D computational model in which the structures of ion channel system are approximated more accurately by tetrahedral meshes conforming the interface between solvent and macromolecule. The conforming meshes are aligned with the "real" ion channel surface, whereas in the lattices method, the mesh is nonconforming because it is allowed to "cut through" the ion channel surface. This will provide advantages of accurately treating proper specification of boundary conditions on the surface and leads to simulation results that are more comparable to experimental results.

In current Poisson-Nernst-Planck model, the finite-size effects are disregarded by treating the solvent and ions as infinitesimal points. There are a number of excellent works that have explored the effects of finite ion size on transport (including PNP) [4, 10, 11, 22, 24, 29, 36, 37, 39, 42, 46]. The steric Poisson-Nernst-Planck [17] is one of typical models accounting for the finite-size effects of ions formulated by the energetic variational approach [12]. It has been observed that the 1D computational results of steric Poisson-Nernst-Planck greatly enhances the selectivity of the ion channel. In the near future, another improvement of the Poisson-Nernst-

Planck model is to implement the 3D computations of steric Poisson-Nernst-Planck [17] taking into account the critical finite-size effects of mobile ions moving through the narrow channel.

Acknowledgement: Minxin Chen, Chun Liu and Shixin Xu are partially supported by NSF grants, DMS-1159937, DMS-1216938 and DMS-1109107. Minxin Chen is also partially supported by the China NSF (NSFC11301368) and the NSF of Jiangsu Province (BK20130278). Sheereen Majd is supported by College of Engineering and Materials Research Institute, Pennsylvania State University. Xingye Yue is partially supported partially by NSF of China under the Grant 11271281. We also want to thank Professor Jinchao Xu for the discussion of Edge Average Finite Element Method.

References

[1] T. W. Allena, M. Hoylesa, S. Kuyucakb, and S. H. Chunga. Molecular and brownian dynamics study of ion selectivity and conductivity in the potassium channel. *Chem. Phys. Lett.*, 313:358–365, 1999.
[2] O. S. Andersen, R. E. Koeppe, and B. Roux. Gramicidin channels. *IEEE T. Nanobiosci.*, 4:295–306, 2005.
[3] H. J. Apell, E. Bamberg, and P. Lauger. Effects of surface charge on the conductance of the gramicidin channel. *Biochem. Biophys. Acta*, 552:369–378, 1979.
[4] A. Archer. Dynamical density functional theory for dense atomic liquids. *J. Phys.: Condens. Matter*, 18:5617, 2006.
[5] I. Babuska. The finite element method for elliptic equations with discontinuous coefficients. *Computing*, 5:207–218, 1970.
[6] R. Capone, S. Blake, M. R. Restrepo, J. Yang, and M. Mayer. Designing nanosensors based on charged derivatives of gramicidin a. *J. Am. Chem. Soc.*, 129:9737–9745, 2007.
[7] A. E. Cardenas, R. D. Coalson, and M. G. Kurnikova. Three-dimensional Poisson-Nernst-Planck theory studies: Influence of membrane electrostatics on gramicidin A channel conductance. *Biophys. J.*, 79:80–93, 2000.
[8] Z. M. Chen and J. Zhou. Finite elemtent methods and their convergence for elliptic and parabolic interface problems. *Numer. Math*, 79:175–202, 1996.
[9] P. G. Ciarlet. *The Finite Element Method for Elliptic Problems*. Elsevier, 1978.
[10] S. Durand-Vidal, J. P. Simonin, and P. Turq. *Electrolytes at Interfaces*. Kluwer, Boston, 2000.
[11] S. Durand-Vidal, P. Turq, O. Bernard, C. Treiner, and L. Blum. perspectives in transport phenomena in electrolytes. *Physica A*, 231:123–143, 1996.
[12] B. Eisenberg, Y. Hyon, and C. Liu. Energy variational analysis of ions in water and channels: Field theory for primitive models of complex ionic fluids. *J. Chem. Phys*, 113:104–127, 2010.
[13] B. Eisenberg and W. S. Liu. Poisson-Nernst-Planck systems for ion channels with permanent charges. *SIAM J. Math. Analysis*, 38(6):1932–1966, 2007.
[14] J. Forster. Mathematical modeling of complex fluids. *master thesis, University of Wurzbur*, 2013.
[15] H. K. Gummel. A self-consistent iterative scheme for one-dimensional steady state transistor calculations. *IEEE T. Electron. Dev.*, 11, 1964.
[16] U. Hollerbach, D. Chen, and R. S. Eisenberg. Two- and three-dimensional Poisson-Nernst-Planck simulations of current flow through gramicidin a. *J. Sci. Comput.*, 16:373–409, 2001.
[17] T. Horng, T. Lin, C. Liu, and B. Eisenberg. Pnp equations with steric effects: A model of ion flow through channels. *J. Phys. Chem. B.*, 116(37):11422–11441, 2012.
[18] H. Hwang, G. C. Schatz, and M. A. Ratner. Incorporation of inhomogeneous ion diffusion coefficients into kinetic lattice grand canonical monte carlo simulations and application to ion current calculations in a simple model ion channel. *J. Phys. Chem.*, 111(49):12506–12512, 2007.
[19] W. Im and B. Roux. Ion permeation and selectivity of OmpF porin: A theoretical study based on molecular dynamics, brownian dynamics and continuum electrodiffusion theory. *J. Mol. Biol.*, 322:851–869, 2002.
[20] M. G. Kurnikova, R. D. Coalson, P. Graf, and A. Nitzan. A lattice relaxation algorithm for three-dimensional Poisson-Nernst-Planck theory with application to ion transport through the gramicidin A channel. *Biophys. J.*, 76:642–656, 1999.
[21] K. Lee, H. Rui, R. W. Pastor, and W. Im. Brownian dynamics simulations of ion transport through the vdac. *Biophys. J.*, 100:611–619, 2011.
[22] L. L. Lee. *Molecular Thermodynamics of Electrolyte Solutions*. World Scientific, Singapore, 2008.
[23] B. Lu, M. J. Holst, A. Mccammon, and Y. C. Zhou. Poisson-Nernst-Planck equations for simulating biomolecular diffusion-reaction processes I: Finite element solutions. *J. Comput. Phys.*, 229:6979–6994, 2010.
[24] B. Lu and Y. C. Zhou. Poisson-Nernst-Planck equations for simulating biomolecular diffusion-reaction processes II: Size effects on ionic distributions and diffusion-reaction rates. *Biophys. J.*, 100:2475–2485, 2011.
[25] M. X. Macrae, S. Blake, X. Jiang, R. Capone, D. J. Estes, M. Mayer, and J. Yang. A semi-synthetic ion channel platform for detection of phosphatase and protease activity. *ACS Nano*, 3:3567–3580, 2009.

[26] M. X. Macrae, S. Blake, M. Mayer, and J. Yang. Nanoscale ionic diodes with tunable and switchable rectifying behavior. *J. Am. Chem. Soc.*, 132:1766–1767, 2010.
[27] M. X. Macrae, D. Schlamadinger, J. E. Kim, M. Mayer, and J. Yang. Using charge to control the functional properties of self-assembled nanopores in membranes. *Small*, 7:2016–2020, 2011.
[28] S. Majd, C. Yusko, A. D. MacBriar, J. Yang, and M. Mayer. Gramicidin pores report the activity of membrane-active enzymes. *J. Am. Chem. Soc.*, 131:16119–16126, 2009.
[29] U. M. B. Marconi and P. Tarazona. Dynamic density functional theory of fluids. *J. Chem. Phys.*, 110:8032, 1999.
[30] S. R. Mathur and J. Y. Murthy. A multigrid method for the Poisson-Nernst-Planck equations. *SIAM J. Appl. Math.*, 52:4031–4039, 2009.
[31] W. Nonner, D. Gillespie, D. Henderson, and B. Eisenberg. Ion accumulation in a biological calcium channel: Effects of solvent and confining pressure. *J. Phys. Chem. B*, 105:6427–6436, 2001.
[32] S. Y. Noskov, W. Im, and B. Roux. Ion permeation through the α-hemolysin channel: Theoretical studies based on brownian dynamics and Poisson-Nernst-Plank electrodiffusion theory. *Biophys. J.*, 87:2299–2309, 2004.
[33] L. Onsager. Reciprocal relations in irreversible processes. I. *Phys. Rev.*, II. Ser. 37:405–426, 1931.
[34] L. Onsager. Reciprocal relations in irreversible processes. II. *Phys. Rev.*, 2:2265–2279, 1931.
[35] P. O. Persson and G. Strang. A simple mesh generator in matlab. *SIAM Rev.*, 46:329–345, 2004.
[36] K. S. Pitzer. *Thermodynamics*. Mcgraw-Hill College, New York, 1995.
[37] K. S. Pitzer and J. J. Kim. Thermodynamics of electrolytes. iv. activity and osmotic coefficients for mixed electrolytes. *J. Am. Chem. Soc.*, 96:5701–5707, 1974.
[38] T. Z. Qian, X. P. Wang, and P. Sheng. A variational approach to the moving contact line hydrodynamics. *J. Fluid Mech.*, 564:333–360, 2006.
[39] G. M. Roger, O. Bernard S. Durand-Vidal, and P. Turq. Electrical conductivity of mixed electrolytes: Modeling within the mean spherical approximation. *J. Phys. Chem. B*, 113:8670–8674, 2009.
[40] B. Roux, T. Allen, Simon Berneche, and W. Im. Theoretical and computational models of biological ion channels. *Q. Rev. Biophys.*, 37:15–103, 2 2004.
[41] T. Schirmer and P. Phale. Brownian dynamics simulation of ion flow through porin channels. *J. Mol. Biol.*, 294:1159–1167, 1999.
[42] G. Stell and C. G. Joslin. The donnan equilibrium a theoretical study of the effects of interionic forces. *Biophys.*, 50:855–859, 1986.
[43] J. W. Strutt. Some general theorems relating to vibrations. *Proc. London Math. Soc.*, IV:357–368, 1873.
[44] V. Thomée. *Galerkin finite element methods for parabolic problems*. Springer, 1997.
[45] B. Tu, M. X. Chen, Y. Xie, L. B. Zhang, B. Eisenberg, and B. Z. Lu. A parallel finite element simulator for ion transport through three-dimensional ion channel systems. *J. Phys. Chem.*, 34(24):2065–2078, 2013.
[46] L. Vrbka, J. Vondrasek, B. Jagoda-Cwiklik, R. Vacha, and P. Jungwirth. Quantification and rationalization of the higher affinity of sodium over potassium to protein surfaces. *P. Natl. Acad. Sci. USA*, 17:15440–15444, 2006.
[47] B. A. Wallace. Structure of gramicidin a. *Biophys. J.*, 49:295–306, 1986.
[48] H. Wu, T. Lin, and C. Liu. On transport of ionic solutions: from kinetic laws to continuum descriptions. *arXiv:1306.3053*, 2014.
[49] J. Xu and L. Zikatanov. A monotone finite element scheme for convection-diffusion equations. *Math. Comp.*, 68:1429–1446, 1999.
[50] S. Xu, P. Sheng, and C. Liu. Energy variational approach for ions transport. *Comm. Math. Sci.*, 12, 1964.
[51] S. Yu and G.W. Wei. Three-dimensional matched interface and boundary (MIB) method for treating geometric singularities. *J. Comput. Phys.*, 227(1):602 – 632, 2007.
[52] C. Yuan, R. J. O'Connell, P. L. Feinberg-Zadek, L. J. Johnston, and S. N. Treistman. Bilayer thickness modulates the conductance of the bk channel in model membranes. *Biophys. J.*, 86:3620–3633, 2004.
[53] Q. Zheng, D. Chen, and G. W. Wei. Second-order Poisson-Nernst-Planck solver for ion transport. *J. Comput. Phys.*, 230:5239–5262, 2011.
[54] Y.C. Zhou, S. Zhao, M. Feig, and G.W. Wei. High order matched interface and boundary method for elliptic equations with discontinuous coefficients and singular sources. *J. Comput. Phys.*, 213(1):1 – 30, 2006.